Nano-Micro Letters

e-ISSN 2150-5551
CN 31-2103/TB

ARTICLE

https://doi.org/10.1007/s40820-024-01560-9

Cite as
Nano-Micro Lett.
(2025) 17:60

Received: 24 July 2024
Accepted: 9 October 2024

Ideal Bi-Based Hybrid Anode Material for Ultrafast Charging of Sodium-Ion Batteries at Extremely Low Temperatures

Jie Bai[1], Jian Hui Jia[1], Yu Wang[1], Chun Cheng Yang[1] ✉, Qing Jiang[1] ✉

HIGHLIGHTS

- Metallic nanoparticles with excellent size controllability and high loading rate are obtained via ultrafast high temperature shock method.
- The Bi/CNRs-15 electrode exhibits an unprecedented rate performance (237.9 mAh g^{-1} at 2 A g^{-1}) at − 60 °C, while the energy density of the full cell can reach to 181.9 Wh kg^{-1} at − 40 °C.
- A novel strategy of high-rate activation is proposed to obtain high capacity and superior stability at low temperature by creating new active sites for interfacial reaction.

ABSTRACT Sodium-ion batteries have emerged as competitive substitutes for low-temperature applications due to severe capacity loss and safety concerns of lithium-ion batteries at − 20 °C or lower. However, the key capability of ultrafast charging at ultralow temperature for SIBs is rarely reported. Herein, a hybrid of Bi nanoparticles embedded in carbon nanorods is demonstrated as an ideal material to address this issue, which is synthesized via a high temperature shock method. Such a hybrid shows an unprecedented rate performance (237.9 mAh g^{-1} at 2 A g^{-1}) at − 60 °C, outperforming all reported SIB anode materials. Coupled with a $Na_3V_2(PO_4)_3$ cathode, the energy density of the full cell can reach to 181.9 Wh kg^{-1} at − 40 °C. Based on this work, a novel strategy of high-rate activation is proposed to enhance performances of Bi-based materials in cryogenic conditions by creating new active sites for interfacial reaction under large current.

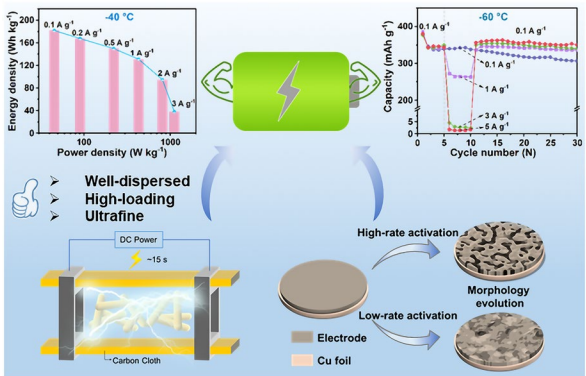

KEYWORDS Bi nanoparticles; High temperature shock; High-rate activation; Ultrafast charging; Low-temperature sodium-ion batteries

✉ Chun Cheng Yang, ccyang@jlu.edu.cn; Qing Jiang, jiangq@jlu.edu.cn
[1] Key Laboratory of Automobile Materials (Jilin University), Ministry of Education, School of Materials Science and Engineering, Jilin University, Changchun 130022, People's Republic of China

Published online: 13 November 2024

1 Introduction

Lithium-ion batteries (LIBs) have accounted for a dominant position in energy storage fields from portable electronic equipment to electric vehicles (EVs) thanks to their high energy density and long lifespan [1–3]. However, severe ionic conductivity decline, sluggish interfacial charge transfer kinetics, fatal dendrite formation and fragile electrolyte/electrode interphase may all deal a crushing blow to the battery performances and safety concerns at subzero temperature, seriously restricting practical applications at high latitudes or altitudes localities, and the fields of civil and military [4–6]. As a consequence, developing advanced energy storage devices with superior temperature tolerance, which could accommodate to the harsh working conditions brought by diverse seasons and regions, is highly desirable. Sodium-ion batteries (SIBs) have gained extensive concerns owing to wide distribution, cost-effectiveness and natural abundance of sodium resources [7–10]. Additionally, Na^+ has smaller de-solvation energy compared with Li^+, demonstrating a lower activation barrier for Na^+ insertion/extraction and thus better electrochemical performances at low temperature [11–13]. Nonetheless, the low operating temperature, especially at high charging rates, could bring decreased ionic conductivity due to increased electrolyte viscosity and unstable interfacial reaction, resulting in severe polarization and capacity decay [14, 15]. So far, the studies of low-temperature SIBs principally focus on modulating the solvation structure and developing electrolytes with low freezing point, which is far from sufficient, let alone the ultrafast charging capability at ultralow temperature [16–18]. In order to promote practical applications of SIBs in cryogenic environments, it is also crucial to enhance the electrode electrochemical performance through structural modification, coating and other strategies [19, 20].

Alloy-type materials, featuring relatively low redox reaction potential and high energy density, have been considered to be promising anode candidates for SIBs [21–23]. Among them, Bi with large lattice spacing [$d_{(003)} = 3.95$ Å], high electronic conductivity (7.8×10^5 S m^{-1}) and theoretical capacity (385 mAh g^{-1}), has attracted great attentions [24, 25]. Wang and coworkers reported that the pure Bi electrode combined with ether-based electrolytes exhibited prospective low-temperature behavior (370 mAh g^{-1} at 0.02 A g^{-1} at − 40 °C) owing to the solvent co-intercalation process [26]. Notwithstanding, the cycling stability and rate performance are still limited at ultralow temperature [27, 28]. Batteries with extremely fast charging capability and long life spans are highly expected on account of the demands for high-power EVs and tools in cold region [29]. It has been proved that designing unique nanostructures is an effective strategy to improve the rate property and cyclability [6, 30, 31]. Thermal treatment is frequently used to fabricate nanomaterials from metal salt precursors. However, the conventional methods based on tube furnace annealing (TFA) generally require relatively long synthesis duration and suffer from low energy utilization efficiency [32, 33]. Uneven heating conditions also give rise to nanoparticle aggregation. Therefore, a rapid and highly effective method for the synthesis of electrode materials is still in high demand. High temperature shock (HTS), a facile and ultrafast synthesis method, has been utilized not only in domains like catalysis, but also in the fabrication of battery electrode materials in recent years [34–37].

Herein, a hybrid of well-dispersed and high-loading Bi nanoparticles embedded in carbon nanorods is fabricated by ultrafast HTS for only 15 s (Bi/CNRs-15), which is demonstrated as an ideal material for ultralow-temperature ultrafast-charging SIBs. The instantaneously generated high temperature can effectively decompose the precursors of metal–organic frameworks (MOFs) to metallic Bi nanoparticles with excellent size controllability and high loading rate. The fast heating and cooling rates inhibit the aggregation of nanoparticles, which considerably shortens the ions/electrons diffusion path. As expected, the designed Bi/CNRs-15 anode displays incredible temperature tolerance, fast charging capability (261.4 mAh g^{-1} at a high rate of 5 A g^{-1}) and cycling stability (241.7 mAh g^{-1} at 1 A g^{-1} after 2400 cycles) at − 40 °C. Even at an extremely low temperature of − 60 °C, the hybrid also delivers a high capacity of 237.9 mAh g^{-1} at 2 A g^{-1}, surpassing all reported SIB anode materials. Furthermore, a stable and homogenous solid-electrolyte interface (SEI) layer with more inorganic species could improve structural stability and boost rate kinetics in some degree, which is unraveled by X-ray photoelectron spectroscopy etching. Moreover, it is worth noting that an unusual phenomenon of capacity increment named "negative fading" takes place after high-rate cycling under low-temperature conditions, which provides a new route to enhance the low-temperature performances of SIBs.

https://doi.org/10.1007/s40820-024-01560-9

2 Experimental Section

2.1 Materials

All chemicals of bismuth chloride ($BiCl_3$, 99%, Macklin Reagent Co., Ltd.), potassium iodide (KI, 99%, Aladdin Reagent Co., Ltd.), acetic acid (CH_3COOH, 99.5%, Macklin Reagent Co., Ltd.), trimesic acid (H_3BTC, 99.9%, Aladdin Reagent Co., Ltd.), methanol (CH_3OH, 99%, Beijing Chemical Works) and dimethylformamide (DMF, 99%, Aladdin Reagent Co., Ltd.) were used without further purification. The ultrapure water used in all experiments was with a specific resistance of 18.2 MΩ cm.

2.2 Preparation of Bi/CNRs-15

First, Bi-MOFs were synthesized via a modified two-step solvothermal method. Typically, $BiCl_3$ (0.5 mmol) and KI (0.5 mmol) were dispersed in acetic acid (50 mL) and deionized (DI) water (12.5 mL), respectively. After fully stirred, these two solutions were mixed to form the tender green suspension and the pH value of the mixture was adjusted to 6. After 30 min of stirring, the above dispersion was transferred into a Polytetrafluoroethylene lined stainless steel autoclave and kept at 160 °C for 2 h. Then BiOI nanosheets (BiOI NSs) were obtained after centrifugation and freeze drying. Subsequently, BiOI NSs (0.5 g) and H_3BTC (0.9 g) were dissolved in the mixture of dimethylformamide (22.5 mL) and methanol (7.5 mL) and magnetically stirred for 30 min. Thereafter, the obtained solution was shifted to a 50 mL Teflon-lined autoclave and held at 120 °C for 3 h. The powders of Bi-MOFs were assembled by filtration, washing and drying. Finally, the carbon cloth loaded with Bi-MOFs was clipped into copper electrodes of DC power to acquire Bi/CNRs-15, which was passed a current of 10 A in the argon-filled glovebox for 15 s. Besides, contrast samples shocked for 5 and 30 s were also synthesized, which are denoted as Bi/CNRs-5 and Bi/CNRs-30, respectively. As a comparison, Bi/CNRs-TFA was synthesized by a conventional TFA treatment. The same Bi-MOF precursors were placed in a tube furnace annealed at 600 °C for 2 h in an Ar/H_2 (with 5 vol% H_2) atmosphere.

2.3 Materials Characterization

X-ray diffraction (XRD) analysis was performed on an instrument with Cu Kα (Rigaku D/Max-2550). Transmission electron microscopy (TEM, JEM-2100F, JEOL) and field-emission scanning electron microscopy (FESEM, JSM-6700F, JEOL) were fulfilled to obtain the structure and morphology of all samples. Raman spectra were carried out by a micro-Raman spectrometer (Renishaw). X-ray photoelectron spectroscopy (XPS) data were collected at an ESCALAB 250Xi system. Thermogravimetric analysis (TGA) was performed in the air using an SDT Q600 instrument. The nitrogen adsorption and desorption (Micromeritics ASAP 2020 analyzer) was used to test the specific surface area and pore sizes. The carbon vacancies were measured by the electron paramagnetic resonance (EPR) technique on a Bruker EMX plusmachine. *In-situ* XRD was performed on a Rigaku Smart lab. Low-temperature electrochemical tests were conducted in the high and low temperature test chamber (BPH-060).

2.4 Electrochemical Measurements

All CR2025-type coin cells were assembled in an argon-filled glove box by employing Na metal as the counter electrode, Whatman glass fiber (GF/C) as the separator, and 1 M $NaPF_6$ in 1,2-dimethoxyethane (DME) as the electrolyte. The active materials (Bi/CNRs-15, Bi/CNRs-5, Bi/CNRs-30, Bi/CNRs-TFA, pure Bi) were mixed with Super P and sodium carboxymethylcellulose with a weight ratio of 7:2:1. The mixed slurry was uniformly pasted on Cu foil and dried in a vacuum oven at 70 °C. Additionally, the mass loadings of active materials were ranging from 0.6 to 4.2 mg cm^{-2}. In this work, all capacities are evaluated by the whole weight of the Bi/CNRs-15 composite. The electrodes were tested 3 cycles at 1 A g^{-1} at room temperature before transferring to the high and low temperature test chamber. The cathode consists of $Na_3V_2(PO_4)_3$ (NVP), Super P and polyvinylidene fluoride in a mass ratio of 7:2:1. The full cell was assembled using NVP and Bi/CNRs-15 as the cathode and anode, respectively, with the same electrolyte and separator. Meanwhile, the voltage range was selected at 1.5–3.3 V for the full cell, and the anode was electrochemically activated for 3 cycles before it was used in the full cell. The galvanostatic charge/discharge and GITT tests were implemented using a

LAND-CT2001A battery testing system in 0.01–1.5 V (*vs.* Na^+/Na) at room temperature/low temperature. The pulse current, duration and relaxation time of the GITT tests are 50 mA g^{-1}, 600 s, and 3600 s, respectively. CV curves and temperature-dependent EIS measurements with a frequency range of 100 kHz to 0.01 Hz were performed on an electrochemical workstation (Ivium-n-Stat).

3 Results and Discussion

3.1 Synthesis and Characterization

The synthesis route of Bi/CNRs-15 is schematically illustrated in Fig. 1a. It has been reported that MOF-based materials present vast opportunities in the quest for optimal electrode materials for rechargeable batteries due to their high porosity, diverse structures and controllable chemical compositions [38–40]. Here, firstly, a Bi-MOF as the precursor (Fig. S1) was prepared by a modified two-step solvothermal reaction [41], in which bismuth chloride ($BiCl_3$)

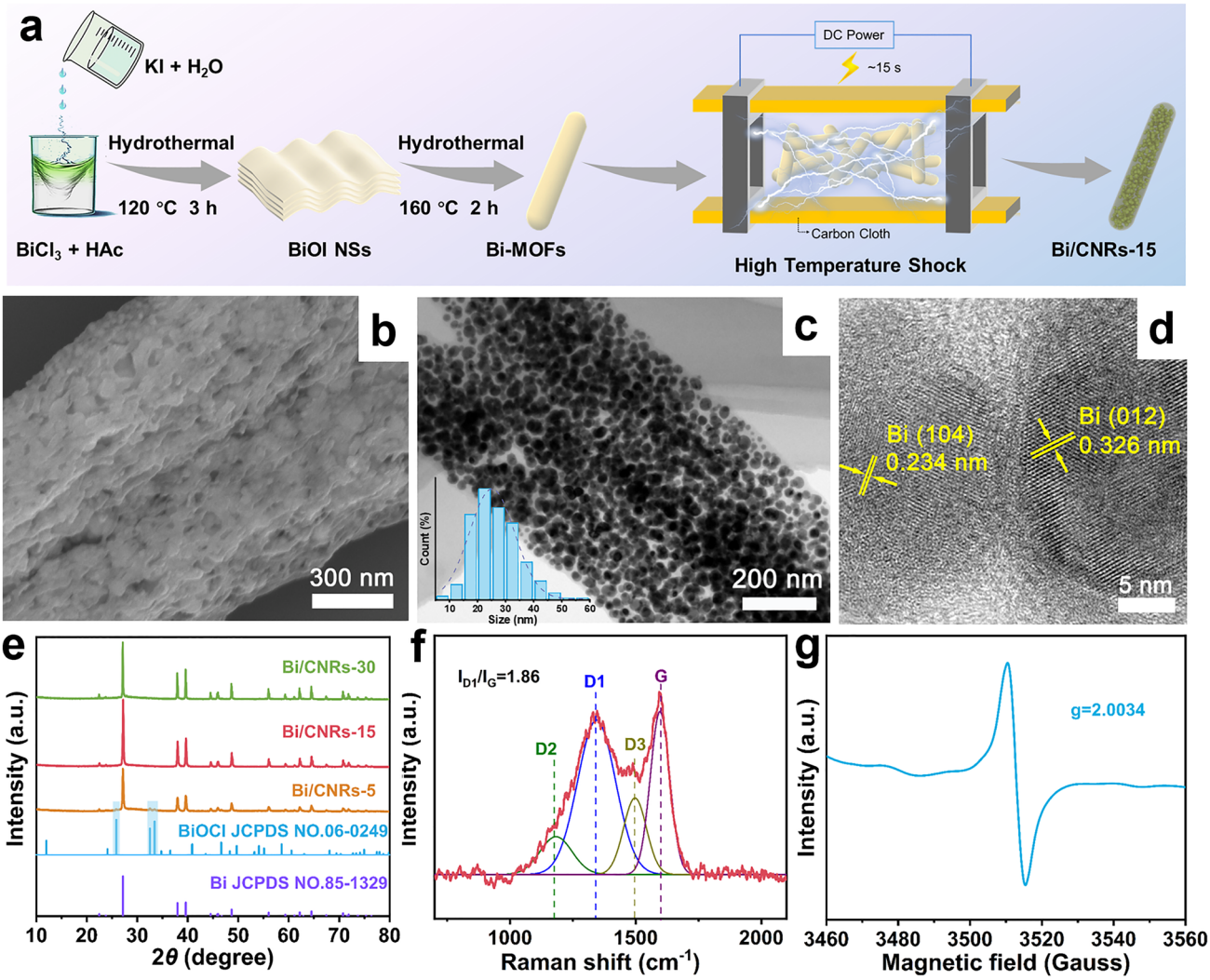

Fig. 1 Schematic illustration and structural morphologies. **a** Schematic illustration of the synthesis route of Bi/CNRs-15. **b** SEM image of Bi/CNRs-15. **c** TEM image of Bi/CNRs-15. **d** HRTEM image of Bi/CNRs-15. **e** XRD patterns of Bi/CNRs-5, Bi/CNRs-15 and Bi/CNRs-30. **f** Raman spectrum of Bi/CNRs-15. **g** EPR spectrum of Bi/CNRs-15

https://doi.org/10.1007/s40820-024-01560-9

as Bi precursor, and the ligand of trimesic acid (H_3BTC) served as a structure-directing agent and carbon source [42]. Specifically, the carboxyl group (–COOH) of H_3BTC lost its proton (H^+) to form the carboxylate ion ($–COO^-$) [43, 44]. Bi^{3+} acted as the central metal ion and coordinated with the $-COO^-$ of the deprotonated H_3BTC ligand to form a coordination bond [43, 45]. After HTS (Fig. S2) in Ar atmosphere for only 15 s, the final product of Bi/CNRs-15 was obtained, where Bi nanoparticles were *in-situ* formed from Bi-MOFs and uniformly embedded in the carbon nanorods. Meanwhile, under the extreme heating generated by HTS, the chlorine can effectively escape from BiOCl (hydrolyzed from $BiCl_3$) through the reaction $2BiOCl + C = 2Bi + CO_2 + Cl_2$ [46]. In order to optimize the synthesis condition, Bi/CNRs-5, Bi/CNRs-30 and Bi/CNRs-TFA were also prepared. All synthesis details are offered in the Experimental Section.

Figures S3 and 1b, c present the field-emission scanning electron microscopy (FESEM) and transmission electron microscopy (TEM) images of Bi/CNRs-15, respectively. Clearly, Bi nanoparticles with an average particle size of 26.5 nm (Fig. S4) are homogeneously loaded in the carbon nanorods, which profits from the rapid cooling/heating rate. In sharp contrast, the analogs of Bi/CNRs-TFA synthesized through a TFA method display aggregated particles, nonuniform size distribution and low metal loading (Figs. S5 and S6), which are principally caused by prolonged heat treatment and slow cooling/heating rate. The samples with different pulse time (5 and 30 s) are also presented in Fig. S7. It is evident that Bi/CNRs-15 exhibits the best dispersity in these three samples. Figure 1d shows the high-resolution TEM (HRTEM) image of Bi/CNRs-15, where highly crystallized nanoparticles can be observed with interlayer distances of 0.326 and 0.234 nm, corresponding to (012) and (104) planes of metallic Bi. The XRD patterns of Bi/CNRs-5, Bi/CNRs-15, Bi/CNRs-30, and Bi/CNRs-TFA are shown in Figs. 1e and S8, respectively. With increasing the thermal shock time, the XRD peaks assigned to BiOCl (JCPDS No. 06-0249) disappear until 15 s and the present sharp peaks are indexed to the high-crystallinity rhombohedral Bi phase (JCPDS No. 85-1329). Note that the average crystallite size of the Bi particles calculated from Scherrer equation (Table S1) is larger than that observed from TEM (26.5 nm). The possible reason is that XRD gives volume-weighted measurements, which tends to overestimate the geometric particle size [47–49]. Moreover, the well-defined crystallinity of Bi/CNRs-15 can be identified by the selected area electron diffraction (SAED) pattern in Fig. S9. A series of clear spotty diffraction rings portray the polycrystallinity of Bi/CNRs-15, further validating the XRD result [50]. As shown in Fig. S10, the bright-field scanning transmission electron microscopy (BF-STEM) and corresponding energy-dispersive spectrum (EDS) mapping images unambiguously reveal that Bi and C elements are homogeneously distributed in the Bi/CNRs-15 composite without obvious aggregation.

XPS was measured to investigate the surface characteristics of the Bi/CNRs-15 hybrid, where only C, Bi, and O elements are perceived (Fig. S11). The high-resolution C 1*s* spectrum (Fig. S12) can be deconvoluted into three peaks at 284.8, 285.7, and 289.2 eV, being ascribed to C–C/C=C, C–O, and C=O bonds, respectively [51]. Two pairs of peaks shown in the Bi 4f high-resolution XPS spectrum (Fig. S13) are assigned to metallic Bi (157.3 and 162.7 eV) and Bi_2O_3 (159.2 and 164.6 eV), resulting from unavoidable oxidation of highly active Bi in the nanoscale under ambient air [22, 27]. After etching 10 nm, the peak intensity of Bi_2O_3 (Fig. S13b) is obviously much weaker than that without etching, proving that Bi_2O_3 mainly exists on the surface of the sample. The high-resolution O 1*s* spectrum (Fig. S14) can be fitted into three peaks with the binding energy of 530.3, 532.4, and 533.9 eV, corresponding to Bi–O, C–O–Bi, and C–O bonds, respectively. The C–O–Bi bond is a chemical bond formed between C and O atoms, and the O atom also interacts with Bi, which involves the coordination of organic ligands to metal ion centers [44]. As observed in the Raman spectrum (Fig. 1f), there are two typical peaks located at 1340 and 1596 cm^{-1}, attributing to D bands (defective structure) and G bands (graphite structure) of carbonous materials, respectively. Moreover, the D band can be further deconvoluted into three peaks at 1345 (D1), 1183 (D2), and 1497 (D3) cm^{-1}, respectively. The D1 band corresponds to the disorders and defects in carbon lattice and the D2 band is ascribed to edge defects, while the D3 band is associated with amorphous sp^3 carbon [52–54]. The calculated ratios of I_{D1}/I_G based on integrated peak intensity is 1.86, disclosing abundant defects and disorders in Bi/CNRs-15. To further corroborate defects in Bi/CNRs-15, electron paramagnetic resonance (EPR) characterization was also carried out. As presented in Figs. 1g and S15, the strong EPR signal at $g = 2.0034$ is associated with the rich carbon vacancies in the Bi/CNRs-15 hybrid [53], which is well consistent

with the Raman spectrum. Compared to Bi/CNRs-TFA, the continuous gas emission can sacrifice irreversible heteroatom defects while induce more reversible carbon vacancies under extreme heating conditions derived from HTS [54]. These abundant vacancies are able to furnish more active sites for the absorption and diffusion of Na^+, which is beneficial for Na storage [55]. The Bi content in Bi/CNRs-15 is determined by the TGA in air, which is calculated to be 86.8% from the equation in Fig. S16. To further study the specific surface area and pore texture type of Bi-MOFs and Bi/CNRs-15, nitrogen adsorption–desorption technique was implemented. As shown in Fig. S17, Bi/CNRs-15 displays a typical mesoporous structure with a specific surface area of 48.1 $m^2 g^{-1}$. The high porosity increases the contact areas between the electrolyte and electrode, and decreases the Na^+ diffusion distance, facilitating the rate performance of Bi/CNRs-15 [56].

3.2 Low-Temperature Performance

The Na storage properties of Bi/CNRs-15 were investigated in 2025 coin-type half cell and full cell at room temperature, which shows remarkable high-rate performance and appealing cycling stability even under high mass loadings (Figs. S18-S27, detailed description in Supporting Information). Based on the well-tailored Bi/CNRs-15 electrode, half cells were also assembled with metallic Na to evaluate the electrochemical performance at low temperature. As shown in Fig. 2a, the Bi/CNRs-15 electrode exhibits admirable adaptability for temperature. The capacity of Bi/CNRs-15 testing at 1 A g^{-1} slightly decreases as the temperature drops to − 40 °C, and the capacity can be retrieved and maintain stability when the temperature returns to 0 °C. The discharge/charge curves (Fig. S29) display polarized plateaus below − 20 °C due to rapidly increasing internal resistance. The CV curves (Fig. S30) under low-temperature conditions show great repetition between the first and second cycles, indicating excellent cycling stability and Na^+ storage reversibility of the Bi/CNRs-15 electrode. From Fig. 2b–d and S31, the Bi/CNRs-15 electrode represents ultrahigh rate capability (261.4 mAh g^{-1} at 5 A g^{-1}) and superior cycling performance (240.3 mAh g^{-1} at 1 A g^{-1} after 2400 cycles with a capacity retention of 67.3%) at − 40 °C, while Bi/CNRs-TFA only exhibits moderate rate property (101.5 mAh g^{-1} at 5 A g^{-1}). In sharp contrast, the pure Bi electrode is unstable and displays battery invalidity after only several cycles at 1 A g^{-1} at − 40 °C (Fig. S32). As presented in Figs. 2e and S33, even at − 60 °C, Bi/CNRs-15 still displays incredible rate property (237.9 mAh g^{-1} at 2 A g^{-1}), which is much better than other anode materials previously reported in open literatures (Fig. 2f and Table S2). Simultaneously, Bi/CNRs-15 also exhibits competitive cycling stability (237.1 mAh g^{-1} at 1 A g^{-1} after 150 cycles) [Fig. 2g]. Surprisingly, the phenomenon of exceeding theoretical capacity appears in Fig. 2b, which has been reported for different kinds of electrode materials (carbon, metal, metal oxide, metal sulfides, etc.) [57–59]. In this work, the extra capacity may come from interfacial charge storage [58]. Additionally, carbonaceous materials can store extra Na in pores and cavities [59].

To preliminarily estimate the practical applications of the Bi/CNRs-15 hybrid in extremely cold areas, the full cell was fabricated using Bi/CNRs-15 as an anode, and NVP as a cathode with a negative/positive (N/P) ratio of 1.01 (see Supporting Information for details) for the electrochemical performance test (Fig. 3a). The Bi/CNRs-15//NVP full cell exhibits excellent fast charging capability at − 40 °C with a high capacity of 382.9 mAh g^{-1} at 0.1 A g^{-1} (based on active mass of the anode), in which 58.9% of the capacity can be retained even when the current density increases by 20-folds from 0.1 to 2 A g^{-1} (Figs. 3b and S34). Note that the specific capacity of the full cell is lower than that of the half cell owing to the un-optimized cathode and the problem of matching the anode and cathode [60]. As illustrated in Fig. S35, the full cell displays appealing cycling stability (a capacity retention of 97.0% at 0.1 A g^{-1} after 100 cycles) after high-rate cycling. As shown in Fig. 3c, the full cell presents a stable capacity retention of 63.9% at 1 A g^{-1} over 1000 cycles. It should be noted that the charged full cell can power the light-emitting diodes (LEDs) at − 40 °C (Figs. 3d and S36). The practical feasibility is further evaluated by the pouch cell (Fig. 3e), which displays 75.8% capacity retention after 100 cycles at 1 A g^{-1}. It should be noted that the coulombic efficiencies of the Bi/CNR-15//NVP pouch cell are lower than 100%, which is caused by the NVP cathode with relatively low CEs of 98.8% and the un-optimized N/P ratio [61, 62]. Figure 3f demonstrates that the assembled full cell delivers a high energy density of 181.9 Wh kg^{-1} at a power density of 45.5 W kg^{-1}, and even 37.9 Wh kg^{-1} at a power density of 1119.5 W kg^{-1} (based on the total mass of the cathode and anode). Even at − 60 °C, the full cell still delivers a capacity of

 https://doi.org/10.1007/s40820-024-01560-9

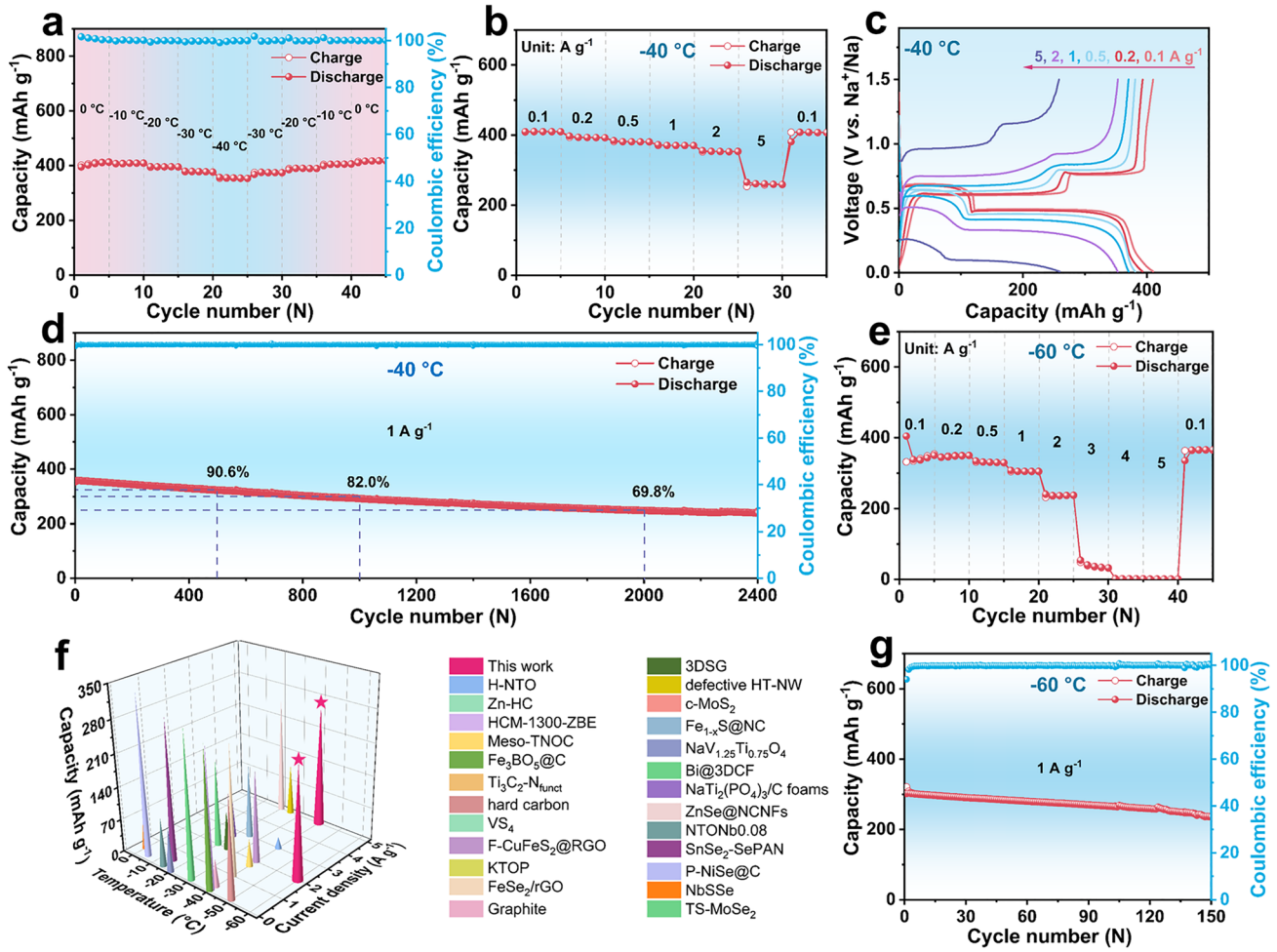

Fig. 2 Half-cell performance at ultralow temperature. **a** Cycling performance of Bi/CNRs-15 at 1 A g^{-1} at different temperatures. **b** Rate performance of Bi/CNRs-15 at − 40 °C. **c** Charge/discharge curves of Bi/CNRs-15 at various rates at − 40 °C. **d** Long-term cycling performance of Bi/CNRs-15 at 1 A g^{-1} at − 40 °C. **e** Rate performance of Bi/CNRs-15 at − 60 °C. **f** Comparisons of rate performance with reported low-temperature SIB anodes. **g** Cycling performance of Bi/CNRs-15 at 1 A g^{-1} at − 60 °C

190.4 mAh g^{-1} at 1 A g^{-1} (Figs. 3g and S37). Totally, the achieved performances illustrate that the as-fabricated Bi/CNRs-15//NVP system possesses outstanding temperature adaptability, fast charging capability, and ultralong lifespan at ultralow temperature, providing evidences of Bi/CNRs-15 as a feasible anode for practical applications in low-temperature SIBs.

3.3 Charge Storage Kinetics

The detailed Na^+ diffusion kinetics of Bi/CNRs-15 and pure Bi were assessed by the galvanostatic intermittent titration technique (GITT) at both 25 and − 40 °C. Clearly, the slope region possesses higher Na^+ diffusion coefficient (D) due to fast Na^+ adsorption on the surface [63], while the plateau region exhibits lower D because of sluggish alloying/dealloying reactions. As the temperature drops to − 40 °C, the D values of Bi/CNRs-15 and pure Bi are in ranges of 1.4×10^{-8} to 7.4×10^{-13} and 1.4×10^{-8} to 3.7×10^{-14}, respectively (Fig. 4a-c). In comparison with pure Bi, the enhanced D values of Bi/CNRs-15 under room temperature (Fig. S41) and low temperature, especially in the plateau region, are well consistent with unprecedented rate capability and also support the positive effect of nanoparticles driven by HTS on the kinetics of Na storage. Moreover, the Bi/CNRs-15 anode presents smaller $\Delta E\tau$ (instantaneous potential change during

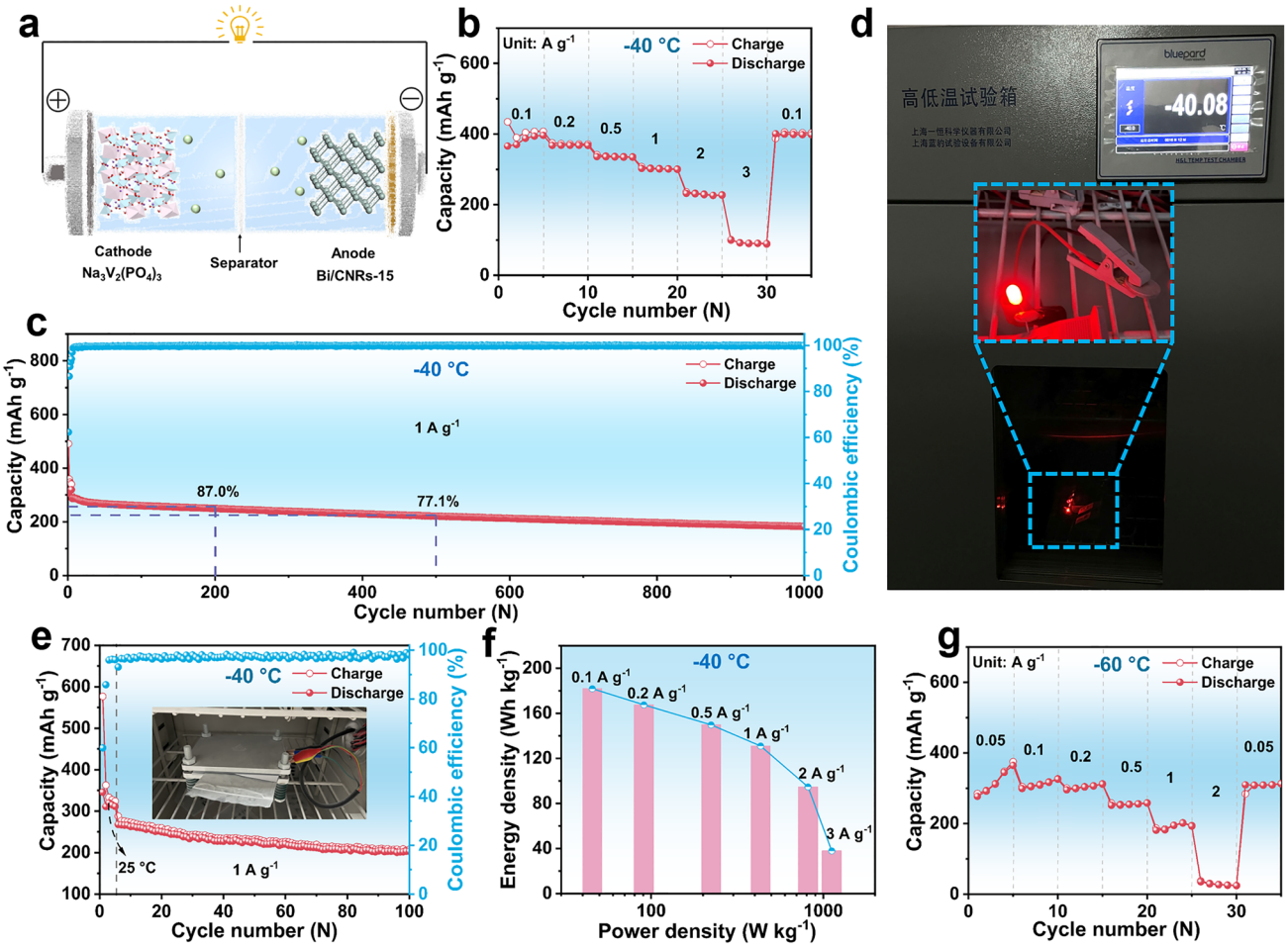

Fig. 3 Full-cell performance at ultralow temperature. **a** The schematic diagram of the full cell with the Bi/CNRs-15 anode and NVP cathode (Bi/CNRs-15//NVP). **b** Rate performance of the Bi/CNRs-15//NVP full cell at −40 °C. **c** Long-term cycling performance of the Bi/CNRs-15//NVP full cell at 1 A g^{-1} at −40 °C. **d** The lighted LEDs driven by the Bi/CNRs-15//NVP full cell at −40 °C. **e** Cycling performance of the Bi/CNRs-15//NVP pouch cell at 1 A g^{-1} at −40 °C. **f** Ragone plot evaluated by the total mass of anode and cathode at −40 °C. **g** Rate performance of the Bi/CNRs-15//NVP full cell at −60 °C

the constant current pulse) and Δ*E*s (steady-state potential change by the current pulse) than the pure Bi anode (Fig. S42), which indicates better Na^+ diffusion ability of Bi/CNRs-15 than pure Bi.

Electrochemical impedance spectroscopy (EIS) measurements were conducted to quantitatively identify the charge transfer resistances and deeply comprehend the superior reaction kinetics of Bi/CNRs-15 [64]. One semicircle in high and middle frequencies and a straight line in low frequency can be observed in the Nyquist plots of Bi/CNRs-15 and pure Bi, implying similitude electrochemical processes in these two electrodes. The fitting results of charge transfer resistance (R_{ct}) and electrolyte resistance (R_{el}) values are quantified with the equivalent circuit. The R_{ct} value decreases gradually with increasing cycles and reaches an extremely low value of 1.2 Ω after 50 cycles (Fig. S43), suggesting that the Bi/CNR-15 electrode has excellent stability and maintains high electrochemical reaction kinetics. As presented in Fig. 4d, compared with room temperature, the steep rise of R_{el} at −40 °C demonstrates low ionic conductivity caused by increased viscosity of the electrolyte [65]. We can also find that R_{ct} of Bi/CNRs-15 is slightly lower than that of pure Bi at 25 °C while much lower at −40 °C, which indicates that Bi/CNRs-15 has a distinct advantage particularly under low-temperature conditions (Fig. 4e). The temperature-dependent EIS was further carried

https://doi.org/10.1007/s40820-024-01560-9

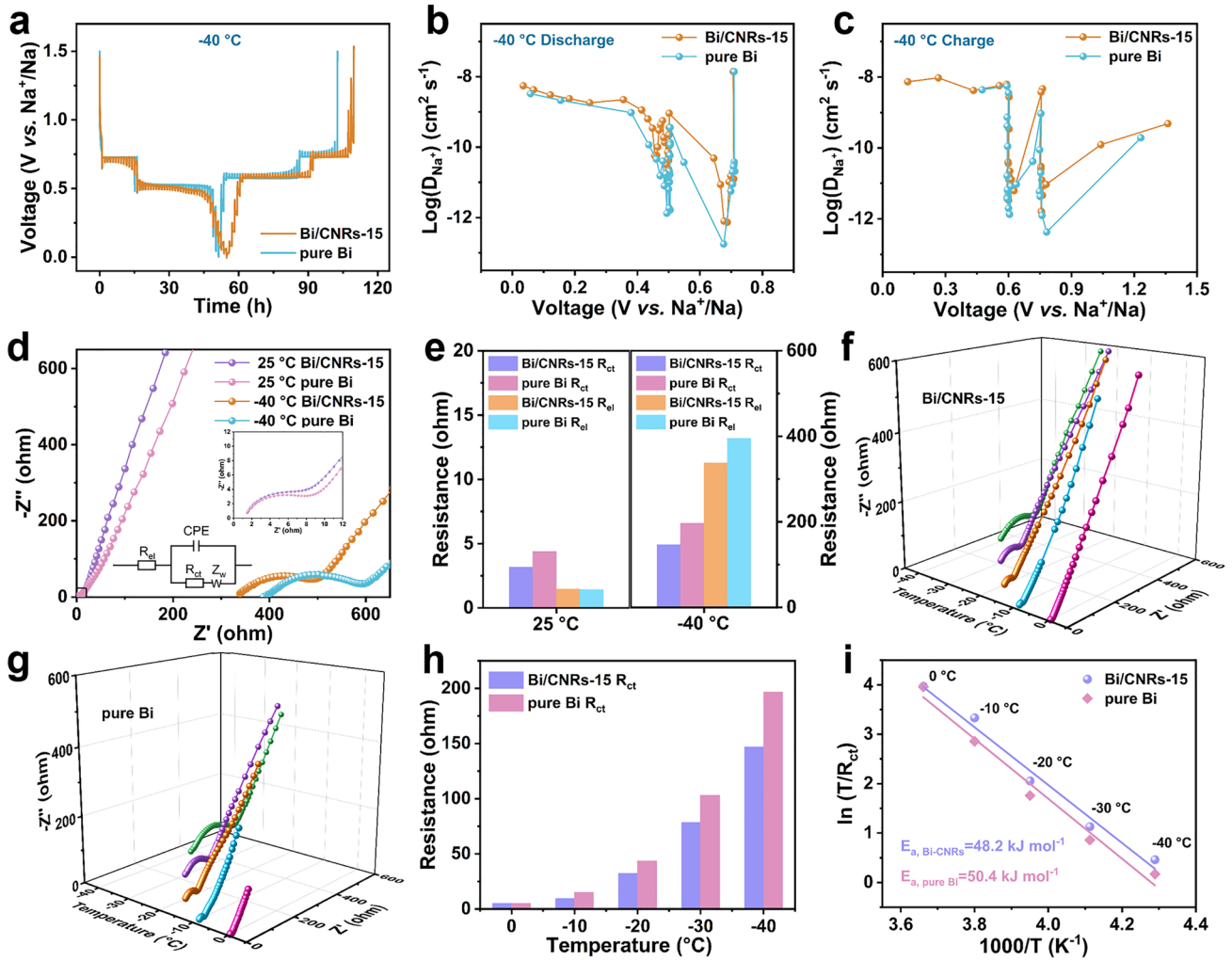

Fig. 4 Electrochemical kinetics analysis at various temperatures. **a** GITT voltage profiles of the Bi/CNRs-15 and pure Bi electrodes at −40 °C. Na^+ diffusion coefficients of Bi/CNRs-15 and pure Bi during the **b** discharging and **c** charging processes at −40 °C. **d** EIS plots of the fresh Bi/CNRs-15 and pure Bi electrodes at 25 and −40 °C, where the inset shows corresponding equivalent circuit diagram and magnified view corresponding to the black box. **e** Comparisons of R_{ct} and R_{el} of the Bi/CNRs-15 and pure Bi electrodes at 25 (left) and −40 °C (right). Temperature-dependent EIS study of **f** Bi/CNRs-15 and **g** pure Bi from −40 to 0 °C. **h** Comparisons of R_{ct} of Bi/CNRs-15 and pure Bi at various temperatures. **i** Arrhenius curves and calculated E_a of Bi/CNRs-15 and pure Bi

out to measure the values of R_{ct} from −40 to 0 °C (Figs. 4f-h and S45). Based on the Arrhenius equation [65, 66],

$$T/R_{ct} = A\exp\left(-E_a/RT\right) \quad (1)$$

where T is the temperature, A is a constant and R is the gas constant. The activation energy (E_a) for charge transfer (Fig. 4i) of Bi/CNRs-15 is calculated to be 48.2 kJ mol^{-1}, which is lower than that of pure Bi (50.4 kJ mol^{-1}). The above results verify that nanomanufacturing and hierarchical porous structure are more conducive to reducing the charge transfer barrier and achieving fast reaction kinetics, which are vital to acquire incredible fast charging capability at extremely low temperature.

3.4 Stable SEI Component

As an inert layer formed from chemical and electrochemical reactions of components in the electrolyte, SEI plays a critical role in determining the performance of batteries [67]. Meanwhile, a cold condition can convert the reaction of electrolyte decomposition and results in the formation

of metastable SEI with dominant organics, which greatly decelerates the migration of Na^+ [68]. In order to further study the relationship between SEI and Na storage behavior, TEM and XPS measurements with different etching depths were carried out for both Bi/CNRs-15 and pure Bi electrodes after 5 cycles at − 40 °C. As shown in Fig. 5a, d, the SEI layer of Bi/CNRs-15 is thin (the thickness of 8–20 nm) and homogeneous, whereas that of pure Bi is thicker (the thickness of 10–42 nm) and uneven. By deeply analyzing the high-resolution spectra of C 1*s*, F 1*s*, and O 1*s* (Figs. 5b, c, e, f and S46), the C 1*s* peaks at 284.8 eV (C–C/C–H), 285.7 eV (C–O), 287.1 eV (C=O), and O 1*s* peaks located at 533.2 eV (C=O) are associated with organic compounds primarily derived from the decomposition of solvents [69, 70]. The peaks at 289.1 eV (Na_2CO_3) of C 1*s* spectra, the peaks located at 529.7 eV (Na_2O) of O 1*s* spectra and the peaks at 684.1 eV (Na-F) are assigned to inorganic components produced from Na^+-solvent-PF_6^- reduction products and the decomposition of $NaPF_6$ [71, 72]. The peaks at 290.6 eV (C-F) of C 1*s* spectra and the peaks located at 689.1 eV (C-F) of F 1*s* spectra illustrate that fluorinated organic compounds reside in SEI layer [73]. A small amount of robust fluorinated organic compounds are highly efficacious to preclude the continuous side reactions of SEI components [74]. As observed in Fig. 5g, h, the concentration of organic species in SEI of pure Bi is commonly higher than that of Bi/CNRs-15, demonstrating more decompositions of solvent existing in the pure Bi electrode. To the extent that the total peak area ratios of Na_2CO_3, Na_2O, and Na-F peaks stand for inorganic species in SEI layer. With increasing etching depths, the proportions of inorganic compounds in SEI on the Bi/CNRs-15 electrode gradually step up and are higher than those in SEI of pure Bi throughout. Specifically, NaF with high lowest unoccupied molecular orbital level and decent band gap is a good electron insulator to block electrons [75]. Na_2CO_3 with relatively high ionic conductivity is conducive to the transport of Na^+ [76]. These two inorganic components can synergize with each other to construct a

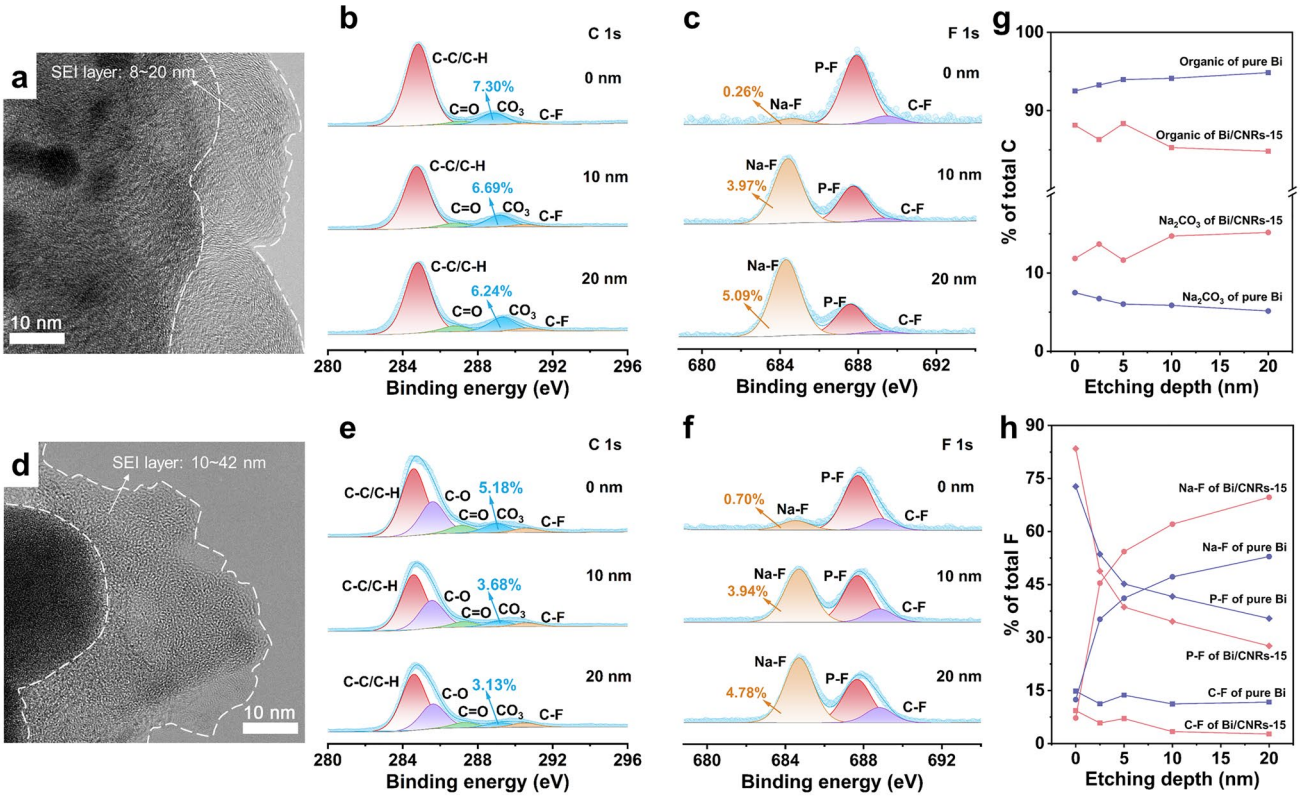

Fig. 5 Surface composition analysis of the Bi/CNRs-15 and pure Bi electrodes operating at − 40 °C. **a** HRTEM image of the Bi/CNRs-15 electrode after 5 cycles at 0.1 A g^{-1}. Depth-profiling XPS spectra of **b** C 1*s* and **c** F 1*s* on the Bi/CNRs-15 electrode. **d** HRTEM image of the pure Bi electrode after 5 cycles at 0.1 A g^{-1}. Depth-profiling XPS spectra of **e** C 1*s* and **f** F 1*s* on the pure Bi electrode. The proportion of SEI components calculated from **g** C 1*s* and **h** F 1*s* spectra

https://doi.org/10.1007/s40820-024-01560-9

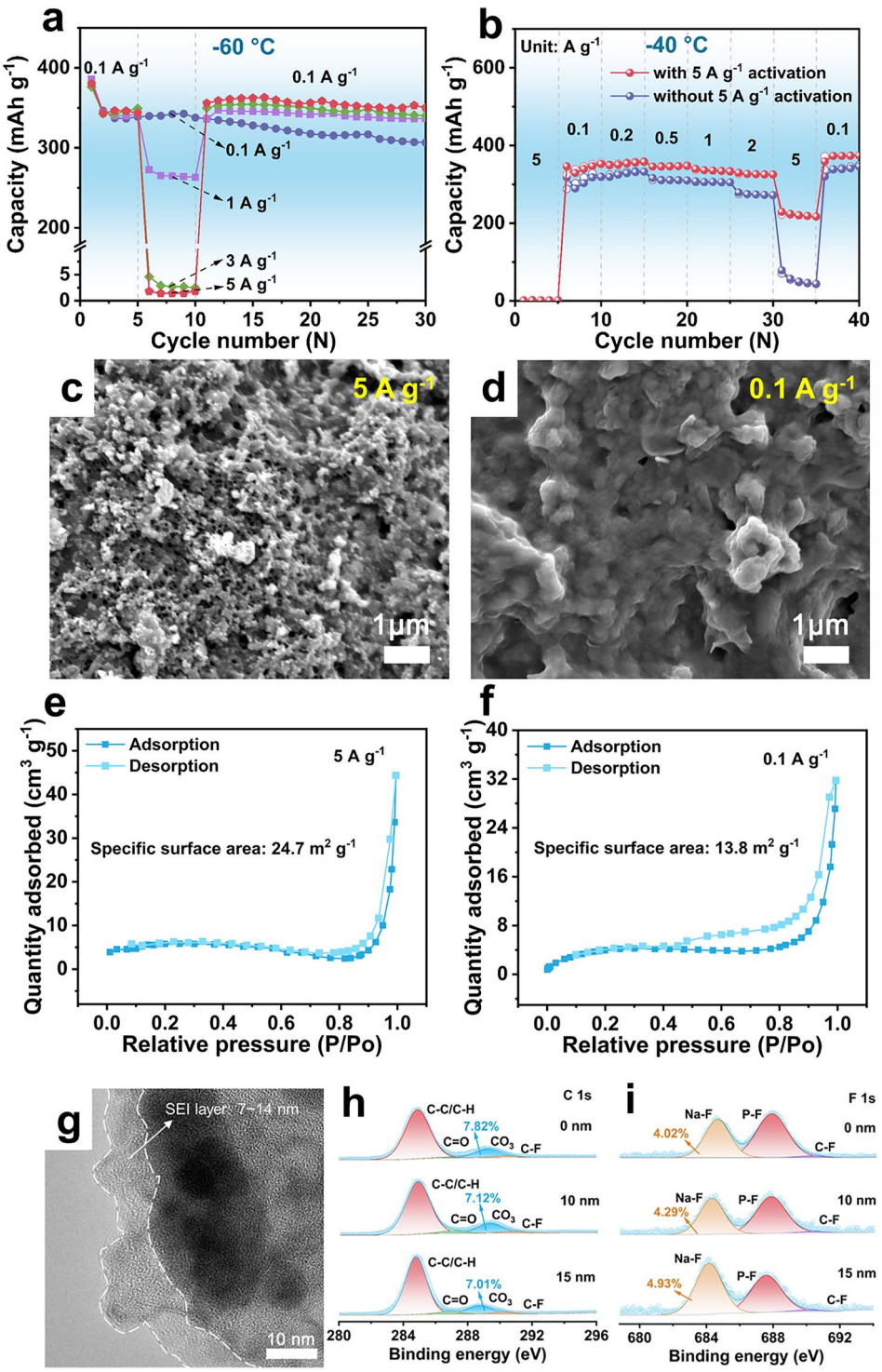

Fig. 6 High-rate activation. **a** Capacity comparisons after high-rate activation (cycled at 0.1 A g^{-1} for 5 times, then 0.1/1/3/5 A g^{-1} for 5 cycles, finally returned to cycling at 0.1 A g^{-1}). **b** Rate performance of Bi/CNRs-15 with a high mass loading (about 1 mg cm^{-2}). **c** SEM image of the Bi/CNRs-15 electrode after 5 cycles at 5 A g^{-1}. **d** SEM image of the Bi/CNRs-15 electrode after 5 cycles at 0.1 A g^{-1}. **e** N_2 adsorption/desorption isotherms of the Bi/CNRs-15 electrode after 5 cycles at 5 A g^{-1}. **f** N_2 adsorption/desorption isotherms of the Bi/CNRs-15 electrode after 5 cycles at 0.1 A g^{-1}. **g** HRTEM image of the Bi/CNRs-15 electrode after 5 cycles at 5 A g^{-1}. Depth-profiling XPS spectra of **h** C 1*s* and **i** F 1*s* on the Bi/CNRs-15 electrode after 5 cycles at 5 A g^{-1}

robust SEI of the anode side. Furthermore, as the sputtering depth increases, the soaring rise in proportion of NaF indicates that the inner SEI layer is mainly composed of inorganic species. The continuous and compact inner SEI layer can effectively buffer the volume expansion and improve the cycling lifetime at low temperature [68]. Overall, more inorganic component in SEI layer on the Bi/CNRs-15 electrode greatly interprets the reason for better rate performance and cycling stability of Bi/CNRs-15 than pure Bi.

3.5 High-Rate Activation

Shockingly, we found that the capacity can be restored and even higher at 0.1 A g^{-1} after losing almost all capacities at 5 A g^{-1} (Fig. 2e). To further explore such an unusual phenomenon named "negative fading", we tested the cycling performance at 0.1 A g^{-1} after high-rate activation (Fig. 6a). Compared with the performance without high-rate activation, Bi/CNRs-15 after high-rate (1/3/5 A g^{-1}) cycling shows capacity increment and stable capacity retention to some extent. The Bi/CNRs-15 electrode with a high mass loading (Fig. 6b) also represents better rate property after high-rate activation at − 40 °C. As shown in Figs. 6c, d, and S47, the electrode activated after high rate of 5 A g^{-1} evolved into smaller-sized coral-like porous nanostructures due to the high mechanical stress during repeated volume changes. To further study the specific surface area of the Bi/CNRs-15 electrode after activation, nitrogen adsorption–desorption test was implemented. It is found that the specific surface area of the Bi/CNRs-15 composite is relatively small (6.8 m^2 g^{-1}, Fig. S48) before activation. However, after 5 cycles at 5 A g^{-1}, the specific surface area of Bi/CNRs-15 composite increases significantly to 24.7 m^2 g^{-1} (Fig. 6e), which is larger than that after 5 cycles at 0.1 A g^{-1} (13.8 m^2 g^{-1}, Fig. 6f). The expanded specific surface area induced by morphology evolution creates additional active sites for interfacial reaction to improve the kinetic properties, resulting in the capacity increment [77, 78]. Ulteriorly, the instantaneous surface activation under large current can dramatically reduce the side reaction between the anode and the electrolyte [79]. The EIS tests were also conducted to further understand the nature behind the excellent electrochemical performance of high-rate activation. As shown in Fig. S49, the value of R_{ct} after 5 cycles at 5 A g^{-1} is only 74.5 Ω, much lower than that after 5 cycles at 0.1 A g^{-1} (174.6 Ω). Figure 6g-i demonstrates that the SEI layer of the Bi/CNRs-15 electrode after 5 cycles at 5 A g^{-1} (the thickness of 7–14 nm) is thinner than that of the Bi/CNRs-15 electrode at 0.1 A g^{-1} (the thickness of 8–20 nm). The dense inorganic species dominate in the inner layer, while a small number of organic compounds are distributed near the surface, showing a layered structure. This is beneficial for Na^+ transfer and enhances the rate capability of the Bi/CNRs-15 electrode after high-rate activation [80, 81]. Overall, due to thinner and more homogeneous SEI layer after high-rate activation and more active sites induced by morphology evolution for redox reaction, the Bi/CNRs-15 electrode after high-rate activation delivers better sodium storage performance. This unique perspective can be used for obtaining high capacity and superior stability of the Bi-based electrodes at low temperature by creating new electrochemically active sites under large current.

4 Conclusions

In this work, a Bi/CNRs-15 hybrid has been elaborately constructed through ultrafast HTS method. The unique HTS process with rapid elevating/quenching rates and short heating time in seconds enables the synthesis of well-dispersed and high-loading ultrafine metallic nanoparticles. As revealed, Bi/CNRs-15 not only exhibits high Na^+ diffusion coefficient, but also possesses low charge transfer activation energy. Being used as the anode material for SIBs, Bi/CNRs-15 displays unprecedented fast-charging ability at ultralow temperature. The full cell (Bi/CNRs-15//NVP) also delivers a high energy density and a promising power density at − 40 °C. Furthermore, a stable and homogenous SEI layer with more inorganic species could improve the structural stability and boost rate kinetics in some degree, which is unraveled by X-ray photoelectron spectroscopy etching. More importantly, an abnormal phenomenon at low temperature of capacity increment named "negative fading" is explored. The guidance of this work makes it possible for further applications of low-temperature fast-charging SIBs.

Acknowledgements This project is financially supported from Science and Technology Development Program of Jilin Province (Nos. 20240101128JC, 20230402058GH), and National Natural Science Foundation of China (No. 52130101).

Authors' Contributions CCY and QJ conceived and designed the project. JB, JHJ and CCY conducted the materials synthesis and

 https://doi.org/10.1007/s40820-024-01560-9

electrochemical tests. JB, YW and CCY contributed to the microstructural characterizations. JB, CCY and QJ wrote the paper. All authors contributed to discussions of the results and have approved the final version of the manuscript.

Declarations

Conflict of interest The authors declare no interest conflict. They have no known competing financial interests or personal relationships that could have appeared to influence the work reported in this paper.

Supplementary Information The online version contains supplementary material available at https://doi.org/10.1007/s40820-024-01560-9.

References

1. H. Jin, S. Xin, C. Chuang, W. Li, H. Wang et al., Black phosphorus composites with engineered interfaces for high-rate high-capacity lithium storage. Science **370**, 192–197 (2020). https://doi.org/10.1126/science.aav5842
2. R.A. House, U. Maitra, M.A. Pérez-Osorio, J.G. Lozano, L. Jin et al., Superstructure control of first-cycle voltage hysteresis in oxygen-redox cathodes. Nature **577**, 502–508 (2020). https://doi.org/10.1038/s41586-019-1854-3
3. D. Lu, R. Li, M.M. Rahman, P. Yu, L. Lv et al., Ligand-channel-enabled ultrafast Li-ion conduction. Nature **627**, 101–107 (2024). https://doi.org/10.1038/s41586-024-07045-4
4. M. Armand, J.-M. Tarascon, Building better batteries. Nature **451**, 652–657 (2008). https://doi.org/10.1038/451652a
5. A. Gupta, A. Manthiram, Designing advanced lithium-based batteries for low-temperature conditions. Adv. Energy Mater. **10**, 2001972 (2020). https://doi.org/10.1002/aenm.202001972
6. N. Zhang, T. Deng, S. Zhang, C. Wang, L. Chen et al., Critical review on low-temperature Li-ion/metal batteries. Adv. Mater. **34**, e2107899 (2022). https://doi.org/10.1002/adma.202107899
7. J.-L. Xia, D. Yan, L.-P. Guo, X.-L. Dong, W.-C. Li et al., Hard carbon nanosheets with uniform ultramicropores and accessible functional groups showing high realistic capacity and superior rate performance for sodium-ion storage. Adv. Mater. **32**, e2000447 (2020). https://doi.org/10.1002/adma.202000447
8. K.H. Shin, S.K. Park, P. Nakhanivej, Y. Wang, P. Liu et al., Biomimetic composite architecture achieves ultrahigh rate capability and cycling life of sodium ion battery cathodes. Appl. Phys. Rev. **7**, 041410 (2020). https://doi.org/10.1063/5.0020805
9. M. Wu, J. Liao, L. Yu, R. Lv, P. Li et al., 2020 roadmap on carbon materials for energy storage and conversion. Chem **15**, 995–1013 (2020). https://doi.org/10.1002/asia.201901802
10. Z. Song, G. Zhang, X. Deng, Y. Tian, X. Xiao et al., Strongly coupled interfacial engineering inspired by robotic arms enable high-performance sodium-ion capacitors. Adv. Funct. Mater. **32**, 2205453 (2022). https://doi.org/10.1002/adfm.202205453
11. T. Hosaka, K. Kubota, A.S. Hameed, S. Komaba, Research development on K-ion batteries. Chem. Rev. **120**, 6358–6466 (2020). https://doi.org/10.1021/acs.chemrev.9b00463
12. W. Zhang, X. Sun, Y. Tang, H. Xia, Y. Zeng et al., Lowering charge transfer barrier of $LiMn_2O_4$ *via* nickel surface doping to enhance Li^+ intercalation kinetics at subzero temperatures. J. Am. Chem. Soc. **141**, 14038–14042 (2019). https://doi.org/10.1021/jacs.9b05531
13. X. Deng, K. Zou, R. Momen, P. Cai, J. Chen et al., High content anion (S/Se/P) doping assisted by defect engineering with fast charge transfer kinetics for high-performance sodium ion capacitors. Sci. Bull. **66**, 1858–1868 (2021). https://doi.org/10.1016/j.scib.2021.04.042
14. J. Qin, Q. Lan, N. Liu, Y. Zhao, Z. Song et al., A metal-free battery working at −80 °C. Energy Storage Mater. **26**, 585–592 (2020). https://doi.org/10.1016/j.ensm.2019.12.002
15. X. Gao, X. Du, T.S. Mathis, M. Zhang, X. Wang et al., Maximizing ion accessibility in MXene-knotted carbon nanotube composite electrodes for high-rate electrochemical energy storage. Nat. Commun. **11**, 6160 (2020). https://doi.org/10.1038/s41467-020-19992-3
16. S. Yuan, T. Kong, Y. Zhang, P. Dong, Y. Zhang et al., Advanced electrolyte design for high-energy-density Li-metal batteries under practical conditions. Angew. Chem. Int. Ed. **60**, 25624–25638 (2021). https://doi.org/10.1002/anie.202108397
17. S. Zhong, Y. Yu, Y. Yang, Y. Yao, L. Wang et al., Molecular engineering on solvation structure of carbonate electrolyte toward durable sodium metal battery at −40 °C. Angew. Chem. Int. Ed. **62**, e202301169 (2023). https://doi.org/10.1002/anie.202301169
18. C. Yang, X. Liu, Y. Lin, L. Yin, J. Lu et al., Entropy-driven solvation toward low-temperature sodium-ion batteries with temperature-adaptive feature. Adv. Mater. **35**, e2301817 (2023). https://doi.org/10.1002/adma.202301817
19. H. Yuan, F. Ma, X. Wei, J.-L. Lan, Y. Liu et al., Solid electrolyte interphases: ionic-conducting and robust multilayered solid electrolyte interphases for greatly improved rate and cycling capabilities of sodium ion full cells (adv. energy mater. 37/2020). Adv. Energy Mater. **10**, 2070153 (2020). https://doi.org/10.1002/aenm.202070153

20. X. Qi, H. Dong, H. Yan, B. Hou, H. Liu et al., Hollow core-shelled $Na_4Fe_{2.4}Ni_{0.6}(PO_4)_2P_2O_7$ with tiny-void space capable fast-charge and low-temperature sodium storage. Angew. Chem. Int. **63**, e202410590 (2024). https://doi.org/10.1002/anie.202410590
21. X. Cheng, Y. Sun, D. Li, H. Yang, F. Chen et al., From 0D to 3D: dimensional control of bismuth for potassium storage with superb kinetics and cycling stability. Adv. Energy Mater. **11**, 2102263 (2021). https://doi.org/10.1002/aenm.202102263
22. R.C. Cui, H.Y. Zhou, J.C. Li, C.C. Yang, Q. Jiang, Ball-*Cactus*-like Bi embedded in N-riched carbon nanonetworks enables the best potassium storage performance. Adv. Funct. Mater. **31**, 2103067 (2021). https://doi.org/10.1002/adfm.202103067
23. S.-L. Wei, Y.-L. Yang, J.-G. Chen, X.-L. Shi, Y. Sun et al., A fast-charging and ultra-stable sodium-ion battery anode enabled by N-doped Bi/BiOCl in a carbon framework. Adv. Energy Mater. (2024). https://doi.org/10.1002/aenm.202401825
24. C. Wang, D. Du, M. Song, Y. Wang, F. Li, A high-power $Na_3V_2(PO_4)_3$-Bi sodium-ion full battery in a wide temperature range. Adv. Energy Mater. **9**, 1900022 (2019). https://doi.org/10.1002/aenm.201900022
25. C. Wang, L. Wang, F. Li, F. Cheng, J. Chen, Bulk bismuth as a high-capacity and ultralong cycle-life anode for sodium-ion batteries by coupling with glyme-based electrolytes. Adv. Mater. **29**, 1702212 (2017). https://doi.org/10.1002/adma.201702212
26. Z. Li, Y. Zhang, J. Zhang, Y. Cao, J. Chen et al., Sodium-ion battery with a wide operation-temperature range from-70 to 100 °C. Angew. Chem. Int. Ed. **61**, e202116930 (2022). https://doi.org/10.1002/anie.202116930
27. L. Liu, S. Li, L. Hu, X. Liang, W. Yang et al., Bi@C nanosphere anode with Na^+-ether-solvent cointercalation behavior to achieve fast sodium storage under extreme low temperatures. Carbon Energy **6**, e531 (2024). https://doi.org/10.1002/cey2.531
28. Y. Wang, X. Xu, Y. Wu, F. Li, W. Fan et al., Facile galvanic replacement construction of Bi@C nanosheets array as binder-free anodes for superior sodium-ion batteries. Adv. Energy Mater. **14**, 2401833 (2024). https://doi.org/10.1002/aenm.202401833
29. Y. Zhang, W. Zhao, C. Kang, S. Geng, J. Zhu et al., Phase-junction engineering triggered built-in electric field for fast-charging batteries operated at −30 °C. Matter **6**, 1928–1944 (2023). https://doi.org/10.1016/j.matt.2023.03.026
30. J. Xu, H. Zhang, F. Yu, Y. Cao, M. Liao et al., Realizing all-climate Li-S batteries by using a porous sub-nano aromatic framework. Angew. Chem. Int. Ed. **61**, e202211933 (2022). https://doi.org/10.1002/anie.202211933
31. S. Xin, Y. You, S. Wang, H.-C. Gao, Y.-X. Yin et al., Solid-state lithium metal batteries promoted by nanotechnology: progress and prospects. ACS Energy Lett. **2**, 1385–1394 (2017). https://doi.org/10.1021/acsenergylett.7b00175
32. M. Guo, Q. Dong, H. Xie, C. Wang, Y. Zhao et al., Ultra-fast high-temperature sintering to avoid metal loss toward high-performance and scalable cermets. Matter **5**, 594–604 (2022). https://doi.org/10.1016/j.matt.2021.11.008
33. M. Cui, C. Yang, S. Hwang, B. Li, Q. Dong et al., Rapid atomic ordering transformation toward intermetallic nanoparticles. Nano Lett. **22**, 255–262 (2022). https://doi.org/10.1021/acs.nanolett.1c03714
34. T. Jiang, Z. Liu, Y. Yuan, X. Zheng, S. Park et al., Ultrafast electrical pulse synthesis of highly active electrocatalysts for beyond-industrial-level hydrogen gas batteries. Adv. Mater. **35**, e2300502 (2023). https://doi.org/10.1002/adma.202300502
35. S. Liu, Y. Shen, Y. Zhang, B. Cui, S. Xi et al., Extreme environmental thermal shock induced dislocation-rich Pt nanoparticles boosting hydrogen evolution reaction. Adv. Mater. **34**, e2106973 (2022). https://doi.org/10.1002/adma.202106973
36. S. Dou, J. Xu, D. Zhang, W. Liu, C. Zeng et al., Ultrarapid nanomanufacturing of high-quality bimetallic anode library toward stable potassium-ion storage. Angew. Chem. Int. Ed. **62**, e202303600 (2023). https://doi.org/10.1002/anie.202303600
37. X. Wu, Z. Li, W. Feng, W. Luo, L. Liao et al., Insights into electrolyte-induced temporal and spatial evolution of an ultra-fast-charging bi-based anode for sodium-ion batteries. Energy Storage Mater. **66**, 103219 (2024). https://doi.org/10.1016/j.ensm.2024.103219
38. L. Zhang, Y. Hou, The Rise and development of MOF-based materials for metal-chalcogen batteries: current status, challenges, and prospects. Adv. Energy Mater. **13**, 2204378 (2023). https://doi.org/10.1002/aenm.202204378
39. S.H. Yang, S.K. Park, Y.C. Kang, MOF-derived $CoSe_2$@N-doped carbon matrix confined in hollow mesoporous carbon nanospheres as high-performance anodes for potassium-ion batteries. Nano-Micro Lett. **13**, 9 (2020). https://doi.org/10.1007/s40820-020-00539-6
40. Z.-L. Zheng, M.-M. Wu, X. Zeng, X.-W. Zhu, D. Luo et al., Facile fabrication of hollow nanoporous carbon architectures by controlling MOF crystalline inhomogeneity for ultra-stable Na-ion storage. Angew. Chem. Int. Ed. **63**, e202400012 (2024). https://doi.org/10.1002/anie.202400012
41. D. Yao, C. Tang, A. Vasileff, X. Zhi, Y. Jiao et al., The controllable reconstruction of Bi-MOFs for electrochemical CO_2 reduction through electrolyte and potential mediation. Angew. Chem. Int. Ed. **60**, 18178–18184 (2021). https://doi.org/10.1002/anie.202104747
42. J. Liu, Z. Wang, P. Cheng, M.J. Zaworotko, Y. Chen et al., Post-synthetic modifications of metal–organic cages. Nat. Rev. Chem. **6**, 339–356 (2022). https://doi.org/10.1038/s41570-022-00380-y
43. Z. Wang, Z. Zeng, H. Wang, G. Zeng, P. Xu et al., Bismuth-based metal–organic frameworks and their derivatives: opportunities and challenges. Coord. Chem. Rev. **439**, 213902 (2021). https://doi.org/10.1016/j.ccr.2021.213902
44. D. Yao, C. Tang, L. Li, B. Xia, A. Vasileff et al., In situ fragmented bismuth nanoparticles for electrocatalytic nitrogen reduction. Adv. Energy Mater. **10**, 2001289 (2020). https://doi.org/10.1002/aenm.202001289

 https://doi.org/10.1007/s40820-024-01560-9

45. X. Yue, L. Cheng, F. Li, J. Fan, Q. Xiang, Highly strained Bi-MOF on bismuth oxyhalide support with tailored intermediate adsorption/desorption capability for robust CO_2 photoreduction. Angew. Chem. Int. Ed. **61**, e202208414 (2022). https://doi.org/10.1002/anie.202208414
46. H. Xie, M. Hong, E.M. Hitz, X.Z. Wang, M.J. Cui et al., High-temperature pulse method for nanoparticle redispersion. J. Am. Chem. Soc. **142**, 17364–17371 (2020). https://doi.org/10.1021/jacs.0c04887
47. T. Li, A.J. Senesi, B. Lee, Small angle X-ray scattering for nanoparticle research. Chem. Rev. **116**, 11128–11180 (2016). https://doi.org/10.1021/acs.chemrev.5b00690
48. M.M. Modena, B. Rühle, T.P. Burg, S. Wuttke, Nanoparticle characterization: what to measure? Adv. Mater. **31**, 1901556 (2019). https://doi.org/10.1002/adma.201901556
49. C. Li, Y.R. Pei, M. Zhao, C.C. Yang, Q. Jiang, Sodium storage performance of ultrasmall SnSb nanoparticles. Chem. Eng. J. **420**, 129617 (2021). https://doi.org/10.1016/j.cej.2021.129617
50. R. Serra-Maia, P. Kumar, A.C. Meng, A.C. Foucher, Y. Kang et al., Nanoscale chemical and structural analysis during *in situ* scanning/transmission electron microscopy in liquids. ACS Nano **15**, 10228–10240 (2021). https://doi.org/10.1021/acsnano.1c02340
51. W.T. Jing, Y. Zhang, Y. Gu, Y.F. Zhu, C.C. Yang et al., N-doped carbon nanonecklaces with encapsulated Sb as a sodium-ion battery anode. Matter **1**, 720–733 (2019). https://doi.org/10.1016/j.matt.2019.03.010
52. Q. Lai, J. Zheng, Z. Tang, D. Bi, J. Zhao et al., Optimal configuration of N-doped carbon defects in 2D turbostratic carbon nanomesh for advanced oxygen reduction electrocatalysis. Angew. Chem. Int. Ed. **59**, 11999–12006 (2020). https://doi.org/10.1002/anie.202000936
53. J. Wang, Y. Yao, C. Zhang, Q. Sun, D. Cheng et al., Superstructured macroporous carbon rods composed of defective graphitic nanosheets for efficient oxygen reduction reaction. Adv. Sci. **8**, e2100120 (2021). https://doi.org/10.1002/advs.202100120
54. Y. Chen, B. Xi, M. Huang, L. Shi, S. Huang et al., Defect-selectivity and "order-in-disorder" engineering in carbon for durable and fast potassium storage. Adv. Mater. **34**, e2108621 (2022). https://doi.org/10.1002/adma.202108621
55. Y.R. Pei, H.Y. Zhou, M. Zhao, J.C. Li, X. Ge et al., High-efficiency sodium storage of $Co_{0.85}Se/WSe_2$ encapsulated in N-doped carbon polyhedron via vacancy and heterojunction engineering. Carbon Energy **6**, 374 (2024). https://doi.org/10.1002/cey2.374
56. X. Yin, Z. Lu, J. Wang, X. Feng, S. Roy et al., Enabling fast Na^+ transfer kinetics in the whole-voltage-region of hard-carbon anodes for ultrahigh-rate sodium storage. Adv. Mater. **34**, e2109282 (2022). https://doi.org/10.1002/adma.202109282
57. H. Long, J. Wang, S. Zhao, B. Zou, L. Yan et al., Enable the domino-like structural recovering in bismuth anode to achieve fast and durable Na/K storages. Angew. Chem. Int. Ed. **63**, e202406513 (2024). https://doi.org/10.1002/anie.202406513
58. Q. Li, H. Li, Q. Xia, Z. Hu, Y. Zhu et al., Extra storage capacity in transition metal oxide lithium-ion batteries revealed by in situ magnetometry. Nat. Mater. **20**, 76–83 (2021). https://doi.org/10.1038/s41563-020-0756-y
59. Z.-S. Wu, G. Zhou, L.-C. Yin, W. Ren, F. Li et al., Graphene/metal oxide composite electrode materials for energy storage. Nano Energy **1**, 107–131 (2012). https://doi.org/10.1016/j.nanoen.2011.11.001
60. L. Jing, K. Zhuo, L. Sun, N. Zhang, X. Su et al., The mass-balancing between positive and negative electrodes for optimizing energy density of supercapacitors. J. Am. Chem. Soc. **146**, 14369–14385 (2024). https://doi.org/10.1021/jacs.4c00486
61. H. Zhang, S. Zhang, B. Guo, L.-J. Yu, L. Ma et al., MoS_2 hollow multishelled nanospheres doped Fe single atoms capable of fast phase transformation for fast-charging Na-ion batteries. Angew. Chem. Int. Ed. **63**, e202400285 (2024). https://doi.org/10.1002/anie.202400285
62. H. Zhang, L. Wang, L. Ma, Y. Liu, B. Hou et al., Surface crystal modification of $Na_3V_2(PO_4)_3$ to cast intermediate $Na_2V_2(PO_4)_3$ phase toward high-rate sodium storage. Adv. Sci. **11**, e2306168 (2024). https://doi.org/10.1002/advs.202306168
63. X. Yi, X. Li, J. Zhong, S. Wang, Z. Wang et al., Unraveling the mechanism of different kinetics performance between ether and carbonate ester electrolytes in hard carbon electrode. Adv. Funct. Mater. **32**, 2209523 (2022). https://doi.org/10.1002/adfm.202209523
64. M. Yousaf, Y. Wang, Y. Chen, Z. Wang, A. Firdous et al., A 3D trilayered CNT/$MoSe_2$/C heterostructure with an expanded $MoSe_2$ interlayer spacing for an efficient sodium storage. Adv. Energy Mater. **9**, 1900567 (2022). https://doi.org/10.1002/aenm.201900567
65. J. Holoubek, H. Liu, Z. Wu, Y. Yin, X. Xing et al., Tailoring electrolyte solvation for Li metal batteries cycled at ultra-low temperature. Nat. Energy **6**, 303–313 (2022). https://doi.org/10.1038/s41560-021-00783-z
66. Y.-S. Hu, Y. Lu, The mystery of electrolyte concentration: from superhigh to ultralow. ACS Energy Lett. **5**, 3633–3636 (2020). https://doi.org/10.1021/acsenergylett.0c02234
67. W. Bai, H. Wang, D.H. Min, J. Miao, B. Li et al., 3D-printed hierarchically microgrid frameworks of sodiophilic Co_3O_4@C/rGO nanosheets for ultralong cyclic sodium metal batteries. Adv. Sci. **11**, e2404419 (2024). https://doi.org/10.1002/advs.202404419
68. S. Weng, X. Zhang, G. Yang, S. Zhang, B. Ma et al., Temperature-dependent interphase formation and Li^+ transport in lithium metal batteries. Nat. Commun. **14**, 4474 (2023). https://doi.org/10.1038/s41467-023-40221-0
69. M. Liu, F. Wu, Y. Gong, Y. Li, Y. Li et al., Interfacial-catalysis-enabled layered and inorganic-rich SEI on hard carbon anodes in ester electrolytes for sodium-ion batteries. Adv. Mater. **35**, e2300002 (2023). https://doi.org/10.1002/adma.202300002
70. G. Yan, K. Reeves, D. Foix, Z. Li, C. Cometto et al., A new electrolyte formulation for securing high temperature cycling and storage performances of Na-ion batteries. Adv. Energy Mater. **9**, 1901431 (2019). https://doi.org/10.1002/aenm.201901431

71. P.M.L. Le, T.D. Vo, H. Pan, Y. Jin, Y. He et al., Excellent cycling stability of sodium anode enabled by a stable solid electrolyte interphase formed in ether-based electrolytes. Adv. Funct. Mater. **30**, 2001151 (2020). https://doi.org/10.1002/adfm.202001151
72. H.S. Hirsh, B. Sayahpour, A. Shen, W. Li, B. Lu et al., Role of electrolyte in stabilizing hard carbon as an anode for rechargeable sodium-ion batteries with long cycle life. Energy Storage Mater. **42**, 78–87 (2021). https://doi.org/10.1016/j.ensm.2021.07.021
73. L. Zhou, Z. Cao, J. Zhang, Q. Sun, Y. Wu et al., Engineering sodium-ion solvation structure to stabilize sodium anodes: universal strategy for fast-charging and safer sodium-ion batteries. Nano Lett. **20**, 3247–3254 (2020). https://doi.org/10.1021/acs.nanolett.9b05355
74. J. Zhang, D.-W. Wang, W. Lv, S. Zhang, Q. Liang et al., Achieving superb sodium storage performance on carbon anodes through an ether-derived solid electrolyte interphase. Energy Environ. Sci. **10**, 370–376 (2017). https://doi.org/10.1039/C6EE03367A
75. E. Wang, J. Wan, Y.-J. Guo, Q. Zhang, W.-H. He et al., Mitigating electron leakage of solid electrolyte interface for stable sodium-ion batteries. Angew. Chem. Int. Ed. **62**, e202216354 (2023). https://doi.org/10.1002/anie.202216354
76. Q. Zhao, S. Stalin, L.A. Archer, Stabilizing metal battery anodes through the design of solid electrolyte interphases. Joule **5**, 1119–1142 (2021). https://doi.org/10.1016/j.joule.2021.03.024
77. H. Sun, G. Xin, T. Hu, M. Yu, D. Shao et al., High-rate lithiation-induced reactivation of mesoporous hollow spheres for long-lived lithium-ion batteries. Nat. Commun. **5**, 4526 (2014). https://doi.org/10.1038/ncomms5526
78. H. Kim, W. Choi, J. Yoon, J.H. Um, W. Lee et al., Exploring anomalous charge storage in anode materials for next-generation Li rechargeable batteries. Chem. Rev. **120**, 6934–6976 (2020). https://doi.org/10.1021/acs.chemrev.9b00618
79. J. Cao, D. Zhang, X. Zhang, Z. Zeng, J. Qin et al., Strategies of regulating Zn^{2+} solvation structures for dendrite-free and side reaction-suppressed zinc-ion batteries. Energy Environ. Sci. **15**, 499–528 (2022). https://doi.org/10.1039/D1EE03377H
80. R. Dong, L. Zheng, Y. Bai, Q. Ni, Y. Li et al., Elucidating the mechanism of fast Na storage kinetics in ether electrolytes for hard carbon anodes. Adv. Mater. **33**, e2008810 (2021). https://doi.org/10.1002/adma.202008810
81. Y. Wan, K. Song, W. Chen, C. Qin, X. Zhang et al., Ultra-high initial coulombic efficiency induced by interface engineering enables rapid, stable sodium storage. Angew. Chem. Int. Ed. **60**, 11481–11486 (2021). https://doi.org/10.1002/anie.202102368

 https://doi.org/10.1007/s40820-024-01560-9